



Development of life assessment procedures for power plant headers operated under flexible loading scenarios

Title	Development of life assessment procedures for power plant headers operated under flexible loading scenarios
Author(s)	Farragher, Tadhg P.;Leen, Sean B.
Publication Date	2013-12-22
Publisher	Elsevier ScienceDirect
Repository DOI	10.1016/j.ijfatigue.2012.12.007

DEVELOPMENT OF LIFE ASSESSMENT PROCEDURES FOR POWER PLANT HEADERS OPERATED UNDER FLEXIBLE LOADING SCENARIOS

T.P. Farragher¹, S. Scully², N.P. O'Dowd³, S.B. Leen¹

¹Mechanical & Biomedical Engineering, Ryan Institute for Environmental, Marine and Energy Research, NUI Galway, Ireland

²ESB Energy International, ESB Head Office, 27 FitzWilliam St., Dublin 2, Ireland

³Department of Mechanical, Aeronautical and Biomedical Engineering, Materials & Surface Science Institute, University of Limerick, Ireland.

Abstract

A finite element methodology for thermomechanical fatigue analysis of a subcritical power plant outlet header under realistic loading conditions is presented. The methodology consists of (i) a transient heat transfer model, (ii) a sequential anisothermal cyclic viscoplastic model and (iii) a multiaxial, critical-plane implementation of the Ostergren fatigue indicator parameter. The methodology permits identification of the local thermomechanical stress-strain response at critical locations and prediction of fatigue life and cracking orientation for complex transient, anisothermal, cyclic elastic-plastic-creep material behaviour. Measured plant data, in the form of steam and pipe temperature transients and steam pressure data, are employed to identify heat transfer constants and validate the predicted thermal response, with particular attention given to plant start-up and attemperation effects. The predictions indicate out-of-phase temperature-strain response at the header inside surface and in-phase response on the outside surface. Cooling transients are predicted to control damage and crack initiation at the inner bore, whereas heating transients are predicted to have a more damaging effect at weld locations. A representative test cycle is presented, which is shown to capture the salient thermo-mechanical cyclic damage of the realistic cycle. The predicted results correlate well with industrial experience in terms of crack (initiation) orientation, location and life.

1. Introduction

There is a need to understand the performance of candidate power plant materials for higher temperatures and pressures. 9-12% Cr steels are an example of such candidate materials, owing to their excellent mechanical properties, and steels such as P91 and P92 are already being utilised in power generation plant [1]. There is an increasing trend towards shifting of energy supply from conventional fossil fuel power plant to sustainable energies, e.g. wind power. To allow for the variable nature of renewable energy supply, there is a requirement to operate existing plant, designed for 'base-load' operation, with relatively infrequent shut-down and start-up, in 'load-following' mode, characterised by increased frequency of shut-down and start-up. This issue has increased the importance of design and assessment of materials and components for high temperature, pressurised plant with respect to thermo-mechanical fatigue (TMF) and creep-fatigue failure.

Current header design does not consider cyclic thermal stresses and load cycling that can lead to creep-fatigue damage [2]. Work carried out in [3] has recognised that repeated start and stop operations lead to creep-fatigue loading on power plant components. In [4], thermo-mechanical modelling of P91 steel in complex power plant geometries, including

1 effects of varying thermal and mechanical loads representative of plant start-up was carried
2 out using an elastic-plastic material model (without strain-rate effects). In [5], [6], [7] the in-
3 service life of 2¹/₄Cr-1Mo steel power plant components has been investigated, based on a
4 linear elastic finite-element analysis, which is expected to underestimate the component
5 lifetime. Lifetime assessment of header geometries under system loading was examined in
6 [8], which highlighted the importance of modelling both the global geometry and local sub-
7 sections of a header geometry.

8 In this work we apply a previously published methodology [9] to a realistic section of a
9 power plant header. This methodology employs temperature dependent material properties in
10 order to capture material behaviour subjected to plant thermal transients during start-up.
11 Realistic loading histories for a high temperature, steam-pressurised P91 pipe, are
12 investigated, in order to predict the thermo-mechanical cyclic behaviour of a P91 steam
13 header with multiple stubs. Finite element (FE) analysis is used to identify critical locations
14 on the header. Mesh refinement, via a submodelling technique, allows for interrogation of
15 these identified critical locations and a life prediction methodology to be implemented. A
16 subsequent representative cycle is then presented which is based upon a simplified version of
17 the realistic cycle. The representative cycle analysis identifies the salient features of a plant
18 operating cycle, to allow rapid but accurate estimates of component life to be obtained.

19 A transient heat transfer model is developed to predict the associated temperature
20 distribution across the wall thickness of a pipe, for subsequent thermo-mechanical analysis.
21 An anisothermal cyclic, elastic-plastic-creep constitutive model is adopted, based on the work
22 presented in [9], to represent the thermo-mechanical response of the material. To determine
23 component lifetime, a multiaxial critical plane (CP) methodology [10] is implemented, using
24 the Ostergren thermomechanical fatigue parameter as a fatigue indicator parameter (FIP). The
25 present work analyses a power plant header undergoing thermally-induced low cycle fatigue
26 (LCF) loading, where the maximum strain and stress may not be coincident due to the non-
27 linear stress-strain response. The Ostergren FIP, which is strain energy based, combines
28 maximum tensile stress with the inelastic strain range [11] for the associated plane, making
29 this FIP suitable for anisothermal high temperature LCF failure.

30 31 32 33 34 35 36 37 **2. Methodology**

38 39 **2.1 General**

40 The overall objective of this work is to develop a lifetime prediction methodology for power
41 plant components subjected to complex thermo-mechanical loading. A key component of the
42 methodology is the ability to predict the thermo-mechanical temperature-stress-strain
43 response of header sections under realistic loading histories. This requires the development of
44 (i) a thermal model which can predict thermal gradients in such components, and (ii) a
45 sequential anisothermal cyclic, viscoplastic constitutive model for the header material. The
46 dimensions of the header correspond to the geometry of an outlet header from a fossil fuel
47 power station in Ireland. A global submodeling technique is employed in order to deliver an
48 efficient but accurate solution to this complex three-dimensional thermomechanical problem.

49 50 51 52 **2.2 Temperature and Loading Histories**

53 Figure 1 shows a set of temperature and pressure time histories, consisting of (i) steam
54 temperature, T_i , during a ‘cold’ plant start-up, (ii) outer wall temperature, T_o , from a steam
55 header during the same time period, (iii) an estimated enclosure temperature-time history, for
56 the building in which the header is situated, and (iv) a steam pressure-time history. This cycle
57 is hereafter referred to as the ‘realistic’ cycle. The steam temperature, T_i , was inferred from a
58 thermocouple attached to a stub pipe; the outer wall temperature, T_o , was measured using a
59
60
61
62
63
64
65

thermocouple attached to the outside surface of the thick walled section of the header. As indicated in Fig. 1, the measured data are only available for the first 20 hours; beyond this, the steam, outside header and enclosure are assumed to cool at a fixed rate.

It can be seen that the steam temperature (blue solid line in Fig. 1) follows the following pattern:

- (i) T_i initially increases from ambient temperature to 398 °C over 2.4 h; T_i remains for a further 8.3 h at an intermediate temperature, which fluctuates about a mean value of approximately 300 °C. (These fluctuations are the result of the attemperation process, where cooling water is injected directly into the steam flow, to control the steam operating temperature).
- (ii) T_i increases gradually, over the next 3 h, to a steady temperature of about 490 °C,
- (iii) T_i stays approximately at this temperature for about 5.8 h
- (iv) T_i returns to ambient temperature at a rate of 13°C/h over 36 h.

The outer wall temperature, T_o , generally lags the steam temperature, T_i , with temperature gradients of up to 150 °C, for example, during heat-up (after about six hours). An exception is between about 5.5 h and 14 h, when quite sudden reductions in steam temperature occur, leading to large temperature gradients through the wall thickness, with a temperature differential between steam temperature and outer wall of up to 100 °C. At the highest steam temperature (490 °C), the wall temperature is about 10 °C cooler than the steam. The steam pressure increases from zero to 17 MPa linearly over the first 4.4 h, the pressure is then held constant for a further 16.8 hrs during which time the plant temperatures eventually stabilises. When the plant enters its cool-down phase the pressure decreases to zero pressure over 1.4 h as the plant shuts down. Two times H_1 and C_1 are annotated in Figure 1; these times correspond to cases when thermal gradients with a hotter inside surface (heating transient, $H_1= 1.974$ hrs) and a cooler inside surface (cooling transient, $C_1 = 7.434$ hrs) occur. The steam header is housed in an enclosure which is heated over time; the enclosure temperature, T_∞ , (indicated by the dash line in Fig. 1) is initially at ambient temperature and increases to 325 °C after initial start-up, and then, following a dwell, lagging that of the steam, increases further to about 475°C, still lagging the steam temperature. As will be seen, this lag between steam temperature and enclosure temperature leads to significant thermal gradient between the inner and outer surfaces of the header during start-up.

A simplified representative cycle (referred to hereafter as the ‘representative’ cycle), is presented in Figure 2, which captures the salient features of the realistic cycle, but without the complex thermal transients shown in Fig. 1. The first part of the representative cycle simulates a start-up to 400 °C and includes one contrived attemperation event. The steam temperature, T_i , increases to 500 °C followed by a linear cooling rate, as in the realistic cycle, the pressure-time history is identical to that of the realistic cycle. In order to conduct a comparison between times H_1 and C_1 of the realistic cycle, times H_2 and C_2 are annotated in Figure 2; these times corresponding to a heating transient ($H_1= 1.974$ hrs) and a cooling transient ($C_1 = 7.4$ hrs) which mirror the transients of the realistic cycle.

2.3 Thermal model

The thermal model employed to simulate the plant cycle is described as follows:

1. A time-dependent steam temperature $T_i(t)$ is specified, based on measured data, (see e.g. Figs. 1 and 2.)

2. A time-dependent enclosure temperature $T_{\infty}(t)$ is specified based on an assumed profile (e.g. Fig. 1), informed by industrial experience, or, where available, outer wall temperature measurement, T_o , is used.
3. Natural convection is modelled on the header external surfaces;
4. Forced steam convection is modelled on the header internal surfaces; Transient heat transfer, with temperature-dependent conductivity and specific heat data, is modelled through the header walls;

The material of the header to be examined is P91; the thermal properties of P91 are presented in Table 1, from [12]. The steam-side convection coefficient is determined from the following equation:

$$Nu = \frac{h_i d}{k}, \quad (1)$$

where h_i is the steam-side forced convection coefficient, k is thermal conductivity and Nu is the Nusselt number, defined in terms of the Prandtl number, Pr , and the Reynolds number, Re , by an empirical correlation [13],

$$Nu = 0.0214(Re^{0.8} - 100)Pr^{0.4} \quad (2)$$

for a smooth pipe with $0.5 < Pr < 1.5$ and $10^4 < Re < 5 \times 10^6$. The Reynolds number, Re , is

$$Re = \frac{\rho u d}{\mu} \quad (3)$$

where ρ is steam density, u is steam velocity, d is the internal pipe diameter and μ is the kinematic viscosity. Here, the steam velocity is taken to be 15 m/s, the recommended velocity to prevent significant pressure drop in long steam pipe lengths [14]. The resulting h_i values for the header surfaces are tabulated in Table 2. The value of h_o was chosen to give the best agreement between predicted and measured outer surface temperature, T_o , seen in Figure 1. The resulting value of $h_o = 1800 \text{ W/m}^2 \cdot \text{K}$ is used for the external surfaces.

2.4 Cyclic Viscoplasticity Model

Isothermal, in-phase (IP) TMF and out-of-phase (OP) test data for P91 are presented in [15] for the temperature range 400 °C to 600 °C, a strain-range of $\pm 0.5\%$ and a strain-rate of $1 \times 10^{-3} \text{ s}^{-1}$. Thermo-mechanical test data for P91 are also presented in [16], covering a broad range of temperature, strain-ranges and strain-rates. A significant effect observed by [16-18], is the phenomenon of cyclic-softening in P91.

In the present work, a material model, known as the two-layer viscoplasticity model [18] is implemented for the P91 material. This material model has been successfully employed for a high temperature forming tool nickel-chrome alloy [19]. The two-layer viscoplasticity model accounts for both rate-dependent (viscoplastic) and rate-independent (plastic) material behaviour. The elasto-plastic network predicts the time-independent behaviour of the material and the elastic-viscous network predicts the time-dependent behaviour of the material due to changes in the applied strain rates. The combination of these two parallel mechanisms will produce the total stress σ ; permanent strain is caused when the yield stress, σ_y , is exceeded, and viscous behaviour, σ_v , is due to viscous effects. The model is implemented within the, FE code ABAQUS [20].

A temperature-dependent version of this two-layer model is adopted here along with a combined non-linear kinematic and isotropic hardening cyclic plasticity model for the time-

independent behaviour and Norton's power law to capture secondary creep. The general equations for the two-layer viscoplasticity model are given below:

$$\boldsymbol{\varepsilon}_p^{el} = \frac{1+\nu}{K_p} \boldsymbol{\sigma}_p - \frac{\nu}{K_p} tr(\boldsymbol{\sigma}_p) \mathbf{I} \quad (4)$$

$$\boldsymbol{\varepsilon}_v^{el} = \frac{1+\nu}{K_v} \boldsymbol{\sigma}_v - \frac{\nu}{K_v} tr(\boldsymbol{\sigma}_v) \mathbf{I} \quad (5)$$

where K_v and K_p are the elastic constants of the elastic-viscous and elastic-plastic networks respectively, ν is Poisson's ratio, \mathbf{I} is unit tensor of second-rank, tr expresses the trace of a tensor, and $\boldsymbol{\sigma}_v$ and $\boldsymbol{\sigma}_p$ are the stress tensors for the elastic-viscous and elastic-plastic networks respectively, defined as:

$$\boldsymbol{\sigma}_v = \mathbf{K}_v : (\boldsymbol{\varepsilon} - \boldsymbol{\varepsilon}_v) \quad (6)$$

$$\boldsymbol{\sigma}_p = \mathbf{K}_p : (\boldsymbol{\varepsilon} - \boldsymbol{\varepsilon}_p) \quad (7)$$

$$\boldsymbol{\sigma} = \boldsymbol{\sigma}_p + \boldsymbol{\sigma}_v \quad (8)$$

where \mathbf{K}_v and \mathbf{K}_p are the elastic tensors of the elastic-viscous and elastic-plastic networks respectively. The yield surface is defined by:

$$f(\boldsymbol{\sigma}_p - \boldsymbol{\alpha}) = \sigma^0 \quad (9)$$

where σ^0 is the current size of the yield surface and $f(\boldsymbol{\sigma}_p - \boldsymbol{\alpha})$ is the equivalent (von Mises) stress, with the back stress $\boldsymbol{\alpha}$, defined as:

$$f(\boldsymbol{\sigma}_p - \boldsymbol{\alpha}) = \sqrt{\frac{3}{2} (\mathbf{S}_p - \boldsymbol{\alpha}^{dev}) : (\mathbf{S}_p - \boldsymbol{\alpha}^{dev})} \quad (10)$$

where $\boldsymbol{\alpha}^{dev}$ is the deviatoric part of the back stress and \mathbf{S}_p is the deviatoric (plastic) stress tensor. The plastic flow rule is

$$\dot{\boldsymbol{\varepsilon}}_p = \frac{\partial f(\boldsymbol{\sigma}_p - \boldsymbol{\alpha})}{\partial \boldsymbol{\sigma}_p} \dot{p} \quad (11)$$

Where \dot{p} is the equivalent plastic strain rate defined as follows:

$$\dot{p} = \sqrt{\frac{2}{3} \dot{\boldsymbol{\varepsilon}}_p : \dot{\boldsymbol{\varepsilon}}_p} \quad (12)$$

The cyclic softening behaviour of the material is captured using an exponential law where the size of the yield surface σ^0 can be defined as a function of equivalent plastic strain, p :

$$\sigma^0 = k + Q_\infty (1 - \exp(-bp)) \quad (13)$$

Here, k is the size of the yield surface at zero plastic strain, and Q_∞ and b are material constants identified from cyclic stress-strain loops, where Q_∞ is the asymptotic value of the stabilised loop and b controls the speed of stabilisation.

The evolution of the kinematic hardening component, according to the generalized Ziegler rule [21] for the anisothermal case, is:

$$\dot{\alpha}_i = C_i \dot{\sigma} \frac{1}{\sigma_0} (\sigma_p - \alpha_i) - \gamma_i \alpha_i \dot{p} + \frac{1}{C_i} \alpha_i \dot{C}_i \quad (14)$$

where $\dot{\alpha}_i$, C_i and γ_i , ($i = 1, 2$) correspond to short strain-range and long strain-range (Frederick-Armstrong) terms respectively. $C_i(T)$ is the temperature-dependent hardening modulus. The individual constants may be identified from the integrated version of the non-linear kinematic hardening equation (see [22]):

$$\frac{\Delta\sigma}{2} - k = \frac{C_i}{\gamma_i} \tanh\left(\gamma_i \frac{\Delta\varepsilon_p}{2}\right) \quad (17)$$

and $\alpha = \alpha_1 + \alpha_2$.

The creep strain is obtained from a Norton power law:

$$\dot{\varepsilon}_v = \frac{3}{2} A [f(\sigma_v)]^n \frac{S_v}{f(\sigma_v)} \quad (15)$$

where A and n are temperature-dependent material constants, $\dot{\varepsilon}_v$ is the viscous creep strain rate and S_v is the deviatoric stress tensor. A parameter B is introduced to define the relative magnitude of K_v , the elastic modulus of the elastic-viscous network, and $K_p + K_v$, the total instantaneous elastic modulus (assumed equal to E , Young's modulus), as follows:

$$B = \frac{K_v}{K_v + K_p} \quad (16)$$

A critical issue in the development of cyclic viscoplasticity models for anisothermal conditions is the identification of the large number of constants required. For the P91 material model used here, the constants are given in Table 3. The identification process has been presented elsewhere [9], including capture of the cyclic softening behaviour, across the 20 °C and 600 °C temperature range and including strain-rate effects via the viscoplasticity formulation

A typical comparison for in-phase and out-of-phase thermomechanical loading for the model is shown in Figs. 3a and 3b, for the isothermally-calibrated material model. The model predictions are compared to data from [15]. The data correspond to a temperature variation between 400 °C and 500 °C and a strain rate of 0.1 % s⁻¹.

In this work, we consider a welded branch connection of a power plant header. Previous work, e.g. [23], has carried out steady-state creep and creep damage analyses of welded branched connections using different Norton and creep damage material parameters for the three weld regions (weld, HAZ and parent metal) in a branched pipe connection. However, as limited data are available for high temperature, cyclic viscoplasticity characterisation of P91

weld metal and heat-affected zones, the current work assumes that the same material parameters can be used to represent weld metal, heat affected zones (HAZ) and parent metal regions. Future work will examine the sensitivity of the predictions to the inclusion of weld and HAZ material properties.

2.5 Global and sub-modelling

A key challenge in the thermomechanical analysis of power plant components is the need to capture complex geometries, including stress concentrations and to provide an accurate representation of time-dependent and possibly non-linear thermal and mechanical response, in practical solution times. To this end, a sub-modelling approach to the thermomechanical analysis is adopted here. The thermomechanical analysis is carried out using the commercial finite-element code ABAQUS [20]. Sub-modelling is used to study a local part of a model with a refined mesh based on interpolation of the solution from an initial, relatively coarse, global model. The global and local submodel geometry for a header with stub-pipe attachments is shown in Figure 4. The global model contains 25,356 eight noded linear brick elements with reduced integration (C3D8R in ABAQUS). The smallest element size is approximately 297 μm in depth. A detailed mesh refinement study was carried out to establish a converged sub-model mesh for the analysis; these analyses established that for the chosen mesh resolution the stresses converged to within 2%. This degree of convergence required 78,276 C3D8R elements with particular refinement focused on the inner bore and the weld region. Sectional views of the relevant regions of the mesh, both global and sub-model, are provided in Figure 5(a) for the sub-model and Figure 5(b) for the global model.

Figure 5 (b) also shows the key header dimensions, with four equally spaced stub pipes intersecting the thick-walled header section. At the stub-header intersection the weld dimensions, although not detailed here, correspond to those of a typical steam header geometry. The lines A, B, C and D, indicated in Figure 5(b) identify locations for data analysis to be presented in Section 3. The first point along path C, in particular, identifies the inner crotch corner, where the stub intersects the main header. Points T_1 and T_2 indicate the approximate location of the thermocouples used to obtain the data in Figure 1.

2.6 Representation of multiaxial fatigue damage

The critical plane approach, e.g. [24], is a method to determine fatigue damage under multiaxial conditions. A chosen fatigue indicator parameter, FIP, is evaluated on all candidate planes, defined in 3D by the angles θ and θ_R , as shown in Figure 6(a). The critical plane is the plane which maximises the FIP. The method can thus predict location, orientation and life for crack initiation under multiaxial conditions. Here the FIP used is the Ostergren parameter, O , such that $O = \Delta\varepsilon_{in}\sigma_{max}$. Here the relevant stress is the stress normal to the plane, as indicated in Figure 6(b) and the strain is the inelastic normal strain range. The procedure is as follows:

1. The stress-strain-time data predicted for a sample candidate material point, using the sub-model of the header, are obtained from the finite-element model
2. For a given candidate plane, defined by θ and θ_R , direction cosines are defined:

$$\begin{aligned} n_y &= -\sin\theta\cos\theta_R \\ n_x &= \sin\theta\sin\theta_R \\ n_z &= \cos\theta \end{aligned} \quad (17)$$

3. The normal stress and strain are calculated for the candidate plane:

$$\sigma_n = \sigma_x n_x^2 + \sigma_y n_y^2 + \sigma_z n_z^2 + 2\tau_{xy} n_x n_y + 2\tau_{yz} n_y n_z + 2\tau_{xz} n_x n_z \quad (18)$$

$$\varepsilon_n = \varepsilon_x n_x^2 + \varepsilon_y n_y^2 + \varepsilon_z n_z^2 + \gamma_{xy} n_x n_y + \gamma_{yz} n_y n_z + \gamma_{xz} n_x n_z \quad (19)$$

4. Steps 2 to 3 are repeated for a given time history response at a given material point for the complete range of candidate planes ($0 \leq \theta < 180^\circ$ and $0 \leq \theta_R < 180^\circ$).
5. The maximum normal inelastic strain range $\Delta\varepsilon_{in}$ and the maximum tensile stress σ_{max} , associated with that strain range, on each particular plane are calculated. This allows for calculation of the Ostergren parameter given as $\Delta\varepsilon_{in}\sigma_{max}$. The plane with the maximum value of O is identified as the critical plane for that material point.
6. The number of cycles to crack initiation for that material point is then predicted using the Ostergren equation:

$$N_f = C(\Delta\varepsilon_{in}\sigma_{max})^\beta \quad (20)$$

where C and β are material constants, independent of temperature.

The value of the Ostergren parameters, C and β , were obtained from data in [17,25] as illustrated in Figure 7. The data of both [17] and [25] show similar trends. However for the purposes of this analysis the constants determined from [17] are used as they provide more conservative results (shorter lives). The constants C and β are found to be 4.5×10^3 and -1.6 , respectively (for stress in units of MPa).

3. Results and Discussion

3.1 Thermal model

The thermal model was validated by comparing measured thermal histories (Figure 1) to predicted temperatures from the FE model. The points selected on the model correspond to the positions from which the measured data were taken in the plant. Figure 8(a) shows the measured and predicted temperature data on the surface of the stub pipe at point T_1 (approximately 150 mm away from the body of the header). Figure 8(b) shows measured and predicted data at point T_2 on the outside surface of the header (a distance 100 mm normal to the plane of the stub pipes). It is clear that the FE model captures the general trends of the measured transients (maximum difference about 35 °C). These results provide confidence in the predicted temperature fields to be used in the thermo-mechanical modelling.

Note that, as a first approximation, the temperature of the outside surface of the stub (from point T_1) can be taken to be equal to the steam temperature, due to the thin wall of the stub, which in turn is close to the inside wall temperature of the header. Hence the difference in temperature between Figure 8(a) and (b) reflect the instantaneous thermal gradient through the wall of the steam header.

The detailed FE thermal analysis provides a more accurate representation of these thermal gradients. For this analysis, two times from the thermal cycle of Figure 1 were selected (H_1 and C_1), as preliminary analysis of the stress strain loops indicated that maximum stresses occurred these times. The temperature distributions at times H_1 and C_1 are depicted in Figures 9(a) and (b), respectively. In both cases there are clearly significant instantaneous thermal gradients, particularly in the regions of the stub-header intersections and the regions between the stubs (ligament regions). The stub pipes show a uniform wall temperature due to the small wall thickness (3.6 mm).

At time H_1 , a typical predicted thermal gradient in a region remote from the pipe stubs is $\Delta T = 117$ °C ($T_i = 323$ °C; $T_o = 215$ °C). At time C_1 , thermal gradients of approximately 75 °C are predicted through the thickness of the header wall..

3.2 Global thermomechanical analysis

The stress distributions along paths A, B, C and D in Figure 5b are examined. The global header model was successfully validated, using a linear elastic material model, against

1 the Lamé solution of a plane strain thick-walled cylinder with a radial thermal gradient
2 (results not shown for brevity).

3 Figure 10 shows the predicted stress profiles from the global non-linear elastic-
4 viscoplastic analysis. The realistic temperature and pressure cycle of Figure 1 is employed.
5 The main effects of introducing the cyclic viscoplasticity material model is the general
6 relaxation (reduction) of peak stresses. Clearly for the heating transient (H_1), high axial (up to
7 ~ 300 MPa) and hoop (up to ~ 170 MPa) stresses are predicted on the outside surface, with
8 path B predicted to experience a high (approximately) equi-biaxial stress state (Figs. 10b and
9 10c). In contrast, for the cooling transient at time C_1 , almost equally high axial and hoop
10 stresses (Figs 10e to 10f) are predicted at the inside surface.

11 Figure 11 shows the predicted von Mises stress distributions from the global elastic-
12 viscoplastic analysis. Significant stress concentrations (grey regions in Figure 11a) are
13 predicted at the inside surface intersection corners (inner crotch corner) and on the outside
14 surface of the header, near the stub pipe junctions. Figure 11b show the von Mises stress
15 contour plot at time C_1 , indicating that the highest stresses are located at the inner crotch
16 corner. This observation is consistent with the work reported in [26], where regions around
17 the stub pipe penetration with the thick-walled header body were reported to experience large
18 thermal stresses, due to rapid changes in the steam temperature, leading to ligament cracking
19 at sites between bore holes. Based on the results of Figure 11, four points of interest were
20 selected for further analysis. These points, as illustrated in Figure 12, are the weld toe saddle
21 and crotch positions and the inner bore saddle and crotch corners.

22 3.3 Sub-model thermomechanical analyses

23 Figure 13a shows the predicted von Mises at time H_1 in the local model. The stress
24 levels in Figure 13(a) may be compared directly with those in the global model (Figure 11a)
25 and it may be noted that the peak stresses are approximately 24% higher, indicating the
26 importance of the sub-model in providing an accurate stress prediction. This von Mises stress
27 is composed of a primarily biaxial stress state with large tensile hoop and axial stresses and
28 comparatively smaller radial stresses. The largest tensile stress was predicted in the axial
29 direction on the outside surface of the header of an approximate magnitude of 346 MPa at the
30 weld toe. Figure 13b shows the von Mises stress distribution at time C_1 . In this case, the peak
31 stresses are predicted on the inside surface of the header, along the stub-header intersection
32 line, extending from the crotch corner to the saddle position. The predicted peak tensile stress
33 occurs in the hoop direction, ~ 281 MPa, at the saddle position. At the inside crotch corner, a
34 tensile stress of ~ 254 MPa is predicted. Hence, biaxial tensile stresses are predicted along
35 this header inner surface edge of the header-stub intersection, leading to tensile plasticity
36 along this edge.

37 Figure 14 shows the predicted thermo-mechanical, stress-strain hysteresis loops for the
38 three normal stress components for the realistic thermal cycle. Figures 14(a) and 14(b)
39 provide the results for the inner bore saddle and crotch, respectively. The trends are
40 remarkably similar, with the peak tensile and compressive stresses (hoop for the saddle and
41 axial for the crotch) corresponding, respectively, to times C_1 and H_1 . For both cases, the
42 thermo-mechanical loops are clearly out-of-phase, i.e. TMF-OP. Significant stress-ranges of
43 443 MPa and 505 MPa are predicted for the saddle and crotch positions, respectively, with
44 tensile stress peaks of 280 MPa and 249 MPa. The corresponding predicted strain ranges are
45 approximately 0.3% and 0.4%, respectively.

46 The predicted thermo-mechanical, stress-strain hysteresis loops for the weld toe saddle
47 and crotch are provided in Figure 14(c) and 14(d), respectively. The weld toe TMF loops are

1 predominantly tensile with tensile mean stresses, the dominant stresses being hoop for the
2 saddle and axial for the crotch. These loops are in-phase, i.e. TMF-IP, with the peak tensile
3 stress/strain corresponding to time H_1 and the peak compressive stress/strain to C_1 . The strain
4 ranges are significantly smaller than those of the weld toe, approximately 0.12% and 0.2%,
5 respectively, for the saddle and crotch and the stress ranges are also smaller than for the weld
6 toe, i.e. about 400 MPa and 500 MPa, respectively, with peak tensile stresses of 275 MPa and
7 340 MPa, respectively. The prediction of a large tensile stress in the axial direction is
8 consistent with the results in [5] pertaining to observed ligament cracking in steam headers.
9

10 Figure 15 present the corresponding TMF hysteresis loops for the representative cycle,
11 for the same four locations. Comparison with the results in Fig. 14 reveal that the predicted
12 stress-strain responses are quantitatively very similar, in terms of stress and strain magnitudes
13 and ranges, in all three directions to those of the realistic cycle.
14

15 **3.4 Thermomechanical fatigue life prediction**

16 A TMF fatigue life analysis was carried out using the approach discussed in Section
17 2.6. Table 4 shows the predicted time to fatigue crack initiation (FCI), based on a position of
18 150 μm from the surface (the location of the closest numerical integration point to the surface
19 in the FE model) for both the realistic and representative cycles. The critical-plane Ostergren
20 approach has been applied, based on maximum values of the stress and inelastic strain ranges
21 over the complete cycle, i.e. neglecting the damage contributions from smaller cycles
22 associated with temperature fluctuations. An alternative approach using a rainflow cycle
23 counting method has also been examined and will be reported in future work [27]. It is clear
24 from Table 4 that the representative cycle gives life predictions very close to those of the
25 realistic cycle. The use of this simplified cycle isolates the key damaging thermal events and
26 provides guidance for scheduling of planned maintenance of power plant.
27

28 The crotch position on the inside (bore) of the header is predicted to be the critical
29 location for crack initiation, with an initiation life of almost 2×10^3 cycles predicted. The
30 predicted orientation of the crack initiation plane indicates that cracking is perpendicular to
31 the longitudinal axis of the header. Assuming one cold start-up per week, which is becoming
32 typical for a fossil-fuel burning plant, with increased use of renewable energy, this
33 corresponds to a crack initiation life of 36.7 years for the realistic cycle. For fatigue crack
34 initiation at the outside surface, which is more easily detected, the crotch position at the weld
35 toe, is the predicted initiation location, after about 3×10^3 cycles (corresponding to 58.3
36 years), which is about 60% longer than for the inside crotch position. Clearly, cracking of the
37 inside surface can be considered more critical, due to the possibilities for steam pressure
38 enhancement of crack growth, corrosion effects and the difficulty in detection of such cracks,
39 without shut-down.
40

41 The predicted results are consistent with industrial observations. For example, ligament
42 bore cracking of a 40 to 45 mm thick economiser header has been observed after 8×10^2 to
43 1×10^3 start cycles [28]. Here, ligament bore cracking is defined as the initiation of
44 longitudinal cracks in the vicinity of the stub pipe-header intersection and the internal header
45 surface interface. It is important to note that the frequency of these cycles was lower than that
46 examined here, so that significant creep damage in addition to LCF is likely to occur. In [28]
47 weld toe crack initiation was reported, followed by radial and circumferential growth, leading
48 to complete fracture of the tube from the header. This is consistent with the observations of
49 [26] where stub weld fracture led to catastrophic failure.
50
51
52
53
54
55
56
57
58
59
60
61
62
63
64
65

4. Conclusions

The accurate prediction of fatigue crack initiation in power plant components is critical for scheduling of plant shutdowns for crack detection. A detailed study of the thermo-mechanical behaviour of a realistic steam header in a fossil fuel power plant has been presented, incorporating multi-axial fatigue damage prediction. The key conclusions are as follows:

- High tensile stresses are predicted (i) on the inside surface during cooling transients and (ii) on the outside surface at the weld toe during heating transients. The predicted behaviour at the inner bore corresponds to out-of-phase temperature-strain cyclic conditions (TMF-OP), whereas conditions at the weld toe correspond to in-phase temperature-cyclic strain (TMF-IP).
- The cooling transient stresses are shown to be more detrimental, leading to predicted crack initiation (using the Ostergren fatigue indicator parameter) within about 1,900 cold start cycles. Outside surface cracking is predicted to occur about 60% later than inside surface cracking. Predicted cracking directions are consistent with reported in-service cracking.
- A simplified, representative cycle, designed to represent the salient features of the significantly more complex realistic cycle, is shown to give almost identical predicted fatigue life and very similar thermo-mechanical cyclic conditions, at the critical location of the header.

5. Acknowledgements

This publication has resulted from research conducted with the financial support of Science Foundation Ireland under Grant Number SFI/10/IN.1/I3015. The authors also wish to acknowledge the SFI/HEA Irish Centre for High-End Computing (ICHEC) for the provision of computational facilities. Helpful discussions with Dr Peter Tiernan of University of Limerick and Prof. Padraic O'Donoghue of NUI, Galway are acknowledged.

6. References

- [1] Viswanathan, R., Purgert, R., Henry, J.F., Tanzosh, J., Stanko, J., Shingledecker, J., and Vitalis, B., 2005. "U.S. Program on materials technology for ultra-supercritical coal power plants," *J Materials Engineering and Performance*, 14(3), 281-292
- [2] Viswanathan, R., 2000. "Life Management of high-temperature piping and tubing in fossil power plants", *Int. J. Pressure Vessels Piping*, 122: 305-316.
- [3] Fournier B., Sauzay M., Caës C., Noblecourt M., Mottot M., Bougault A., Rabeau V., Pineau A., 2008. "Creep-fatigue-oxidation interactions in a 9Cr-1Mo martensitic steel. Part I: Effect of tensile holding period on fatigue lifetime", *Int. J. Fatigue*, 30:649-662
- [4] Okrajni J., Junak G., Marek A., 2008. "Modelling of the deformation process under thermo-mechanical fatigue conditions", *Int. J. Fatigue*, 30: 324-329
- [5] Kwon, O., Myers, M., Karstensen, A.D., Knowles, D., 2006. "The effect of the steam temperature fluctuations during steady state operation on the remnant life of the superheater header", *Int. J. Pressure Vessels Piping*, 83:349-358
- [6] Mukhopadhyay, N.K., Dutta, B.K., Kushwaha, H.S., 2000. "A finite element program for on-line assessment of critical plant components- On-line fatigue-creep monitoring for high-temperature components of power plant", *Int. J. Fatigue*, 23:549-560
- [7] Samal, M.K., Dutta, B.K., Guin, S., Kushwaha, H.S., 2009. "A finite element program for on-line assessment of critical plant components", *Engineering Failure Analysis*, 16:85-111.

- 1
2
3
4
5
6
7
8
9
10
11
12
13
14
15
16
17
18
19
20
21
22
23
24
25
26
27
28
29
30
31
32
33
34
35
36
37
38
39
40
41
42
43
44
45
46
47
48
49
50
51
52
53
54
55
56
57
58
59
60
61
62
63
64
65
- [8] Calonius, K., Cronvall, O., Junninen, P., 2007. "Structural analysis and lifetime assessment of outlet headers", *Baltica VII, Life management and maintenance of power plants*. Vol.1.
 - [9] Farragher, T.P., Scully, S. O'Dowd, N.P. Leen, S.B., 2012. "Thermomechanical analysis of a pressurised pipe under plant conditions", *Trans. ASME. J. Pressure Vessel Technology*. In press.
 - [10] Bong-Ryul. Y., Soon-Bok. L., 1996. "A critical review on multiaxial fatigue assessments of metals", *Int. J. Fatigue*. 18:235-144.
 - [11] Ostergren, W. J., 1967. "A damage foundation hold time and frequency effects in elevated temperature low cycle fatigue", *J. Test Eval*. 4:327-339.
 - [12] ASME., 1995. ASME B31.1 Code for Pressure Piping, ASME, NY.
 - [13] Holman J. P., 2002. Heat Transfer, 9th Edition, McGraw-Hill, New York.
 - [14] Steam Engineering Principles and Heat Transfer., 2011. www.spiraxsarco.com.
 - [15] Saad A. A., Hyde C. J., Sun W., Hyde T. H., 2011. "Thermal-mechanical fatigue simulation of a P91 steel in a temperature range of 400-600°C", *Materials at High Temperature* 28 (3), 212-218.
 - [16] Fournier B., Sauzay M., Caës C., Noblecout M., Mottot M., 2006. "Analysis of the hysteresis loops of a martensitic steel Part I: Study of the influence of strain amplitude and temperature under pure fatigue loadings using an enhanced stress partitioning method", *J. Materials Science and Engineering*, 183-196
 - [17] Ebi, G., McEvily, A.J., 1984. "Effect of processing on the high temperature low cycle fatigue properties of modified 9Cr-1Mo ferritic steel", *Fatigue Engng Mater. Struct*, Vol. 7: 299-314.
 - [18] Kichenin J., Dang Van K., 1996. "Finite-element simulation of a new two-dissipative mechanisms model for bulk medium-density polyethylene", *J. Material Science*, 31: 1653-1661
 - [19] Deshpande A., Leen, S.B., Hyde T. H., 2010. "Experimental and numerical characterisation of the cyclic thermomechanical behaviour of a high temperature forming tool alloy", *Trans ASME, J. Manufacturing Science and Engineering*; 132:1-11.
 - [20] 2010, ABAQUS User and Theory Manuals, Version 6.10, Dassault Systemes.
 - [21] Ziegler, H., 1959. A modification of Parger's hardening rule. *Q. Appl. Mech.* 17,55-65.
 - [22] Lemaitre J., Chaboche J., 1990. Mechanics of Solid Materials, Cambridge University Press, UK.
 - [23] Rayner, G, Hyde, TH, Leen, SB, Sun,W, "Parametric analysis of stresses in welded branched pipes under creep conditions", *Proc Instn Mech. Engrs, Part L: J. Materials Design & Applications*, Vol 219, No L4, pp 231-248, 2005.
 - [24] Das, J., Sivakumar, S.M., 1999. "An evaluation of multiaxial fatigue life assessment methods for engineering components", *Int. J. Pressure Vessels Piping*, 76:741-746.
 - [25] Nagesha, A., Valsan, M., Kanna, R., Bhanu Sankara Rao, K., Mannan, S.L., 2002. "Influence of temperature on the low cycle fatigue behaviour of a modified 9Cr-1Mo ferritic steel", *Int. J. Fatigue*, Vol 24;1285-1293.
 - [26] Nakonezny, G.J., Schultz, C.C., 1995. "Life assessment of high temperature headers", *American Power Conference*.
 - [27] Farragher, T.P., Scully, S. O'Dowd, N.P. Leen, S.B., "A thermomechanical analysis methodology for power plant components", In preparation 2012.
 - [28] Paterson, I. R., Wilson, J. D., 2002. "Use of damage monitoring systems for component life optimisation in power plant", *Int. J. Pressure Vessel and Piping.*, 79: 541-547.

Table 1. Temperature dependent heat transfer properties for P91[12].

Property	20 C	200 C	400 C	600 C
Density (kg/m ³)	7860	7860	7860	7860
Conductivity (W/mK)	22.5	26.2	27.7	27.7
Specific heat capacity (J/kg K)	440	510	600	770

Table 2. Calculated steam-side convection heat transfer coefficients.

Header region (Internal surfaces)	h_i (W/m ² .K)
Stub pipes	4786
Thick-walled pipe	3611

Table 3. Identified temperature-dependent NLKH and viscoplastic constants for P91.

T	k [4,15]	E [18]	Q_∞ [15]	b [15]	A [15]	n [15]	C_1 [4,15]	γ_1 [4, 15]	C_2 [4, 15]	γ_2 [4, 15]	B
°C	MPa	MPa	MPa		MPa hr ⁻¹		MPa		MPa		
20	166	213000	–	–	–	–	374999	790	0	0	0
223	159	198791	–	–	–	–	363500	791	0	0	0
400	95	183938	-55	0.45	0.000134	2.25	352500	2350	48600	405.0	0.2
500	90	165882	-60	0.6	1.62E-05	2.54	215872	2191	48235	460.7	0.41
600	85	140700	-75.4	1	6.31E-06	2.7	106860	2055	31159	463.0	0.54

Table 4. Results of multiaxial critical-plane analyses for selected locations of interest on representative TMF header simulation showing crack orientation and cycles to fatigue crack indication for both realistic plant cycle (Fig 1) and representative plant cycle (Fig 2).

Region	Location	Angle θ	Angle θ_R	FCI Realistic (cycles)	FCI Realistic (years*)	FCI Representative (cycles)	FCI Representative (years*)
Weld toe	Saddle	90	90	3508	67.5	3624	69.7
	Crotch	0	90	3032	58.3	3093	59.5
Bore	Saddle	90	90	1998	38.4	2178	41.9
	Crotch	0	90	1910	36.7	1954	37.6

*based on assumption of one cold start cycle per week.

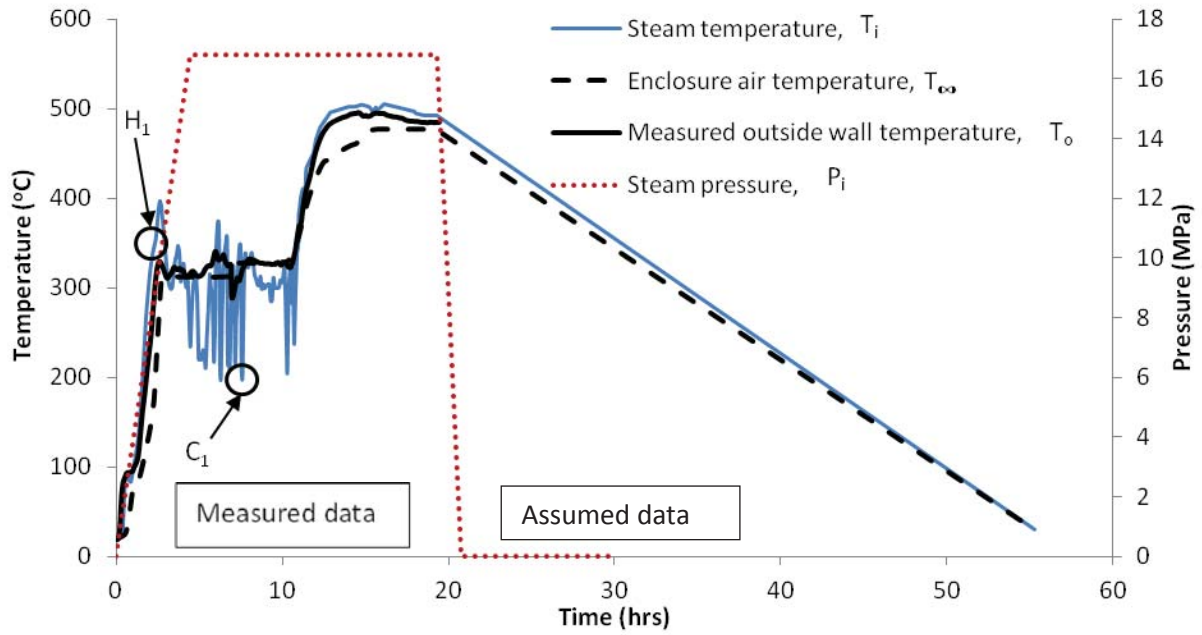


Figure 1 Realistic cold start cycle, based on measured plant data.

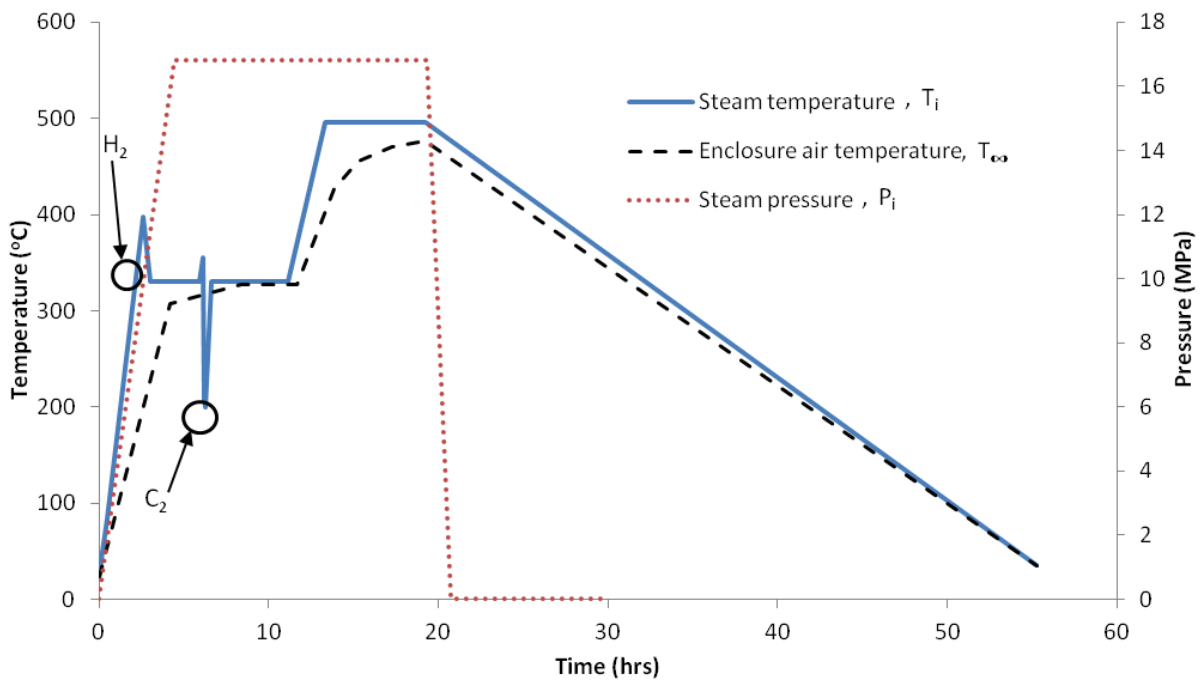


Figure 2. Representative cold-start cycle for plant header conditions, designed to mimic salient thermo-mechanical damaging plant conditions.

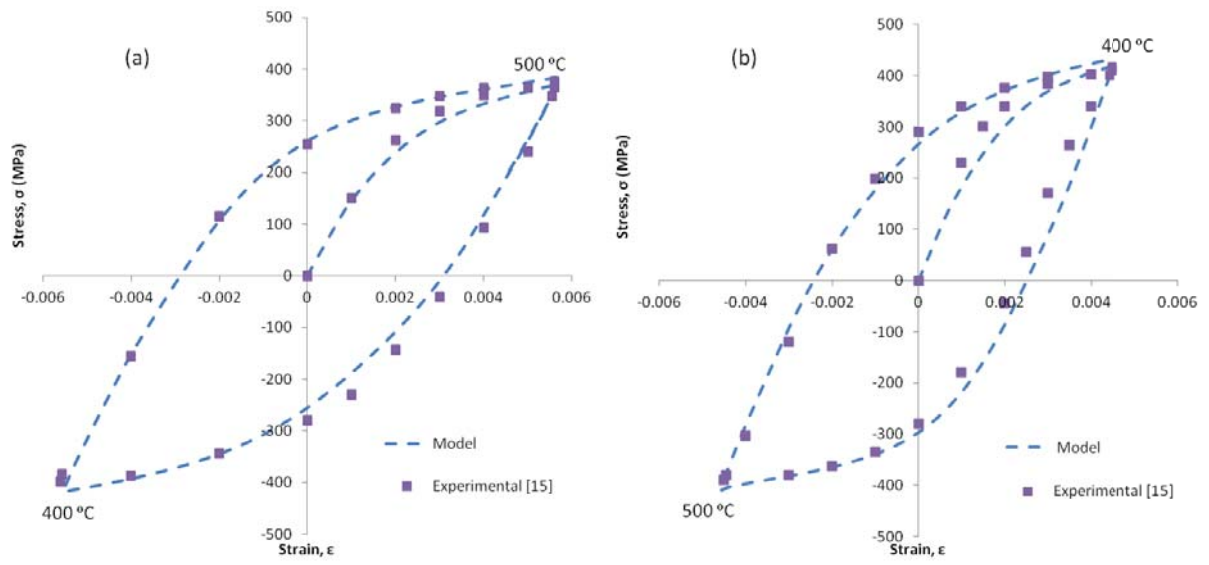


Figure 3. Comparison of predicted and measured ([16]) uniaxial, anisothermal cyclic stress-strain curves for P91 material for TMF-IP (a) and TMF-OP (b) between 400 °C and 500 °C.

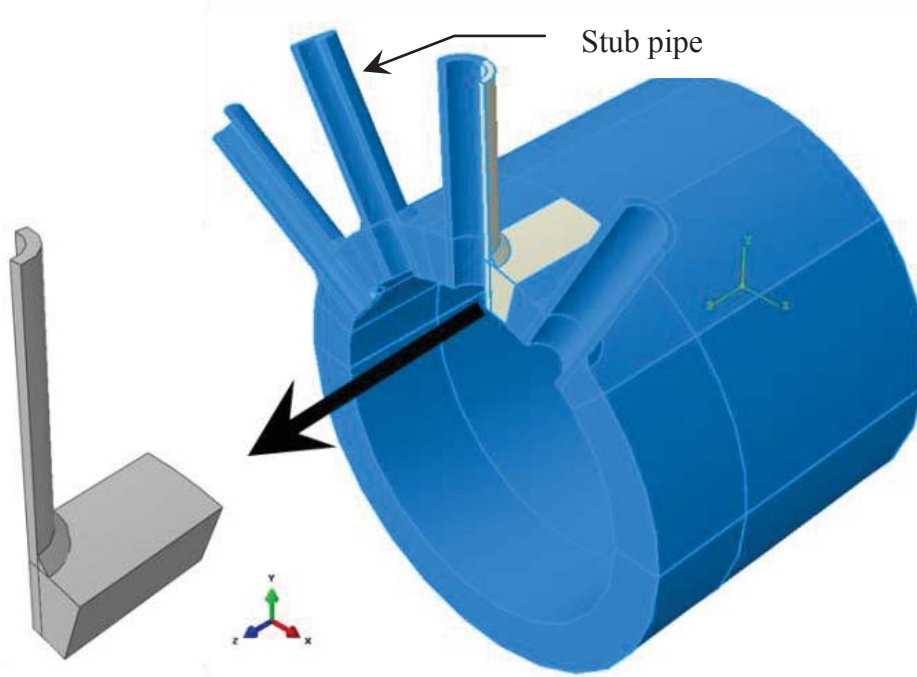


Figure 4. Depiction of submodel position relative to global model.

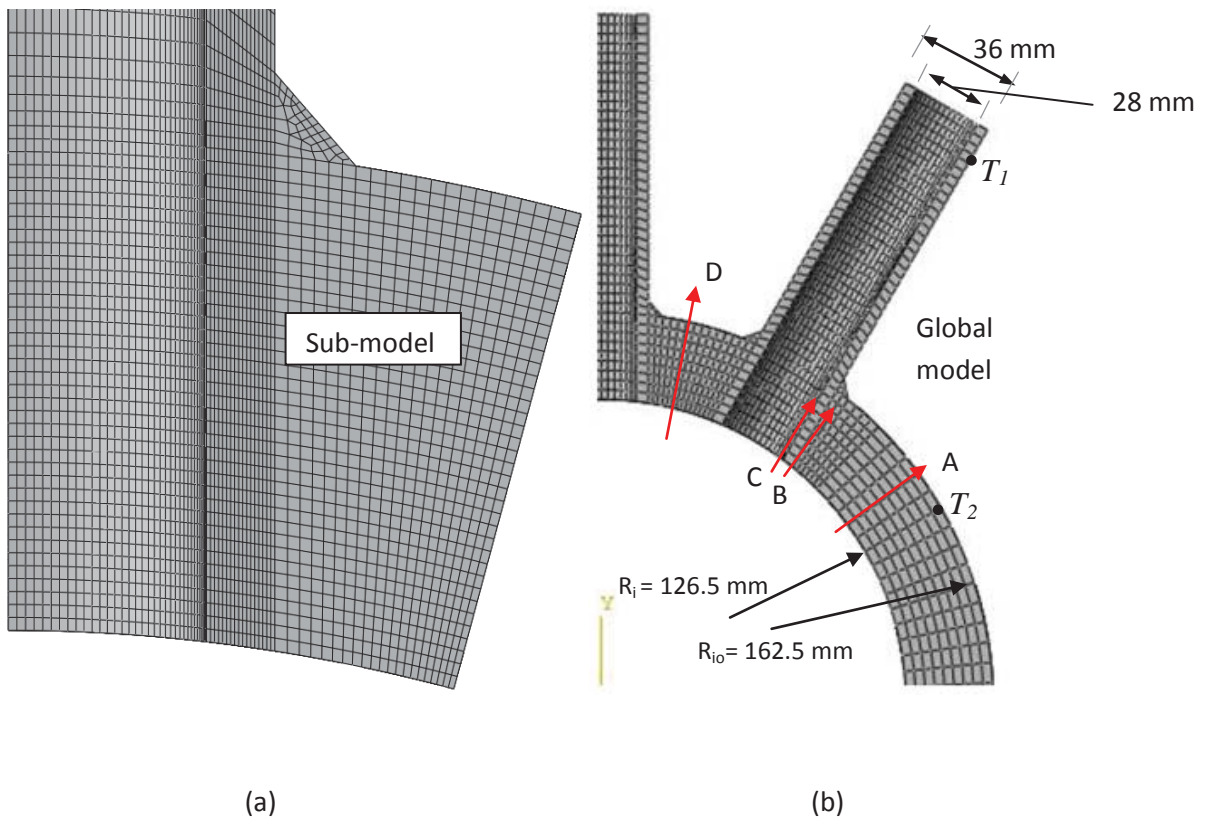


Figure 5. Detail of mesh refinement in (a) inner bore region of sub-model and (b) global model. Also shown are header through-thickness paths for sampling of stress distributions.

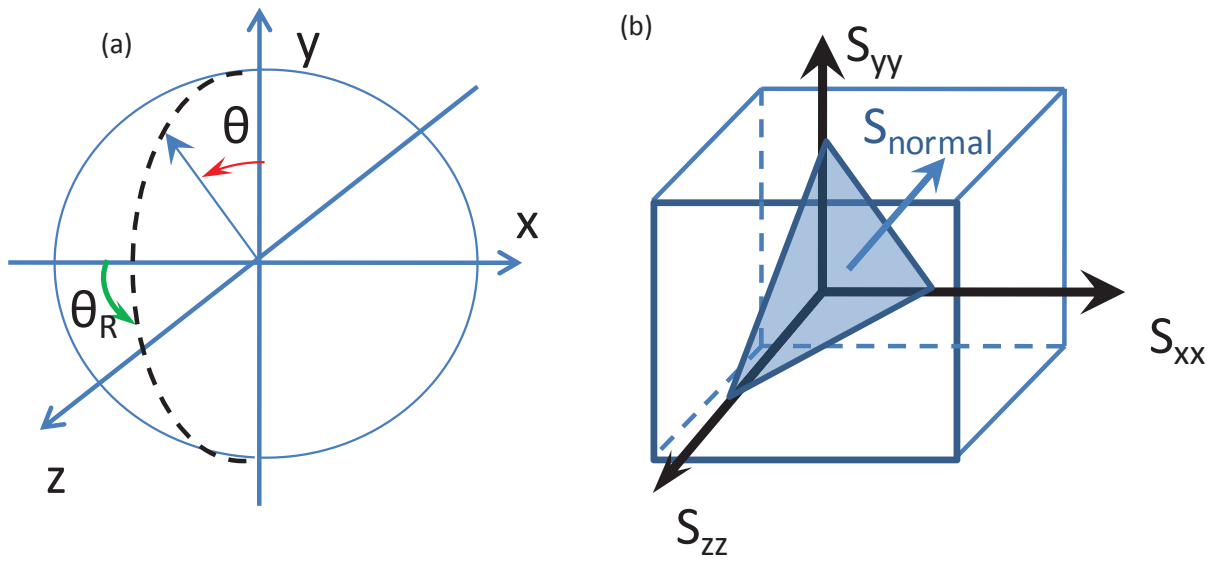


Figure 6. (a) Graphical definition of θ and θ_R for a typical material point of interest, (b) normal stress vector to identified critical plane.

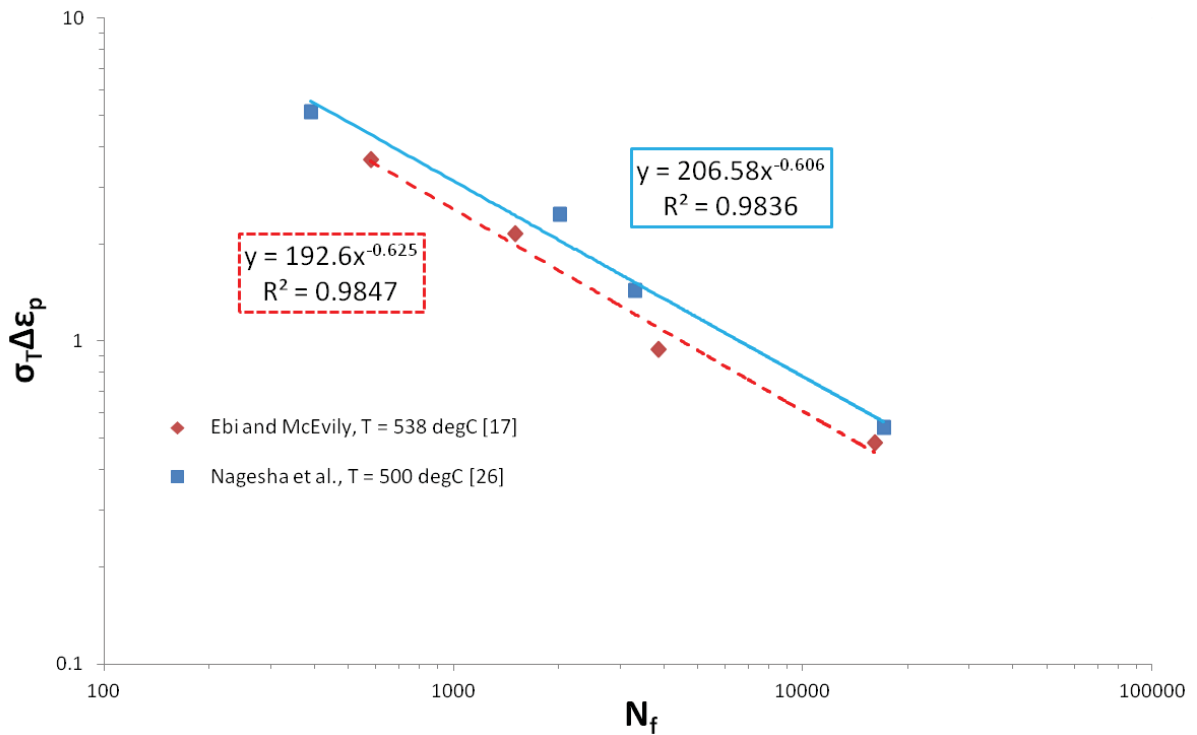


Figure 7. Calibration of Ostergren TMF parameter against test data from [25] for 500 degC and [17] for 538 degC.

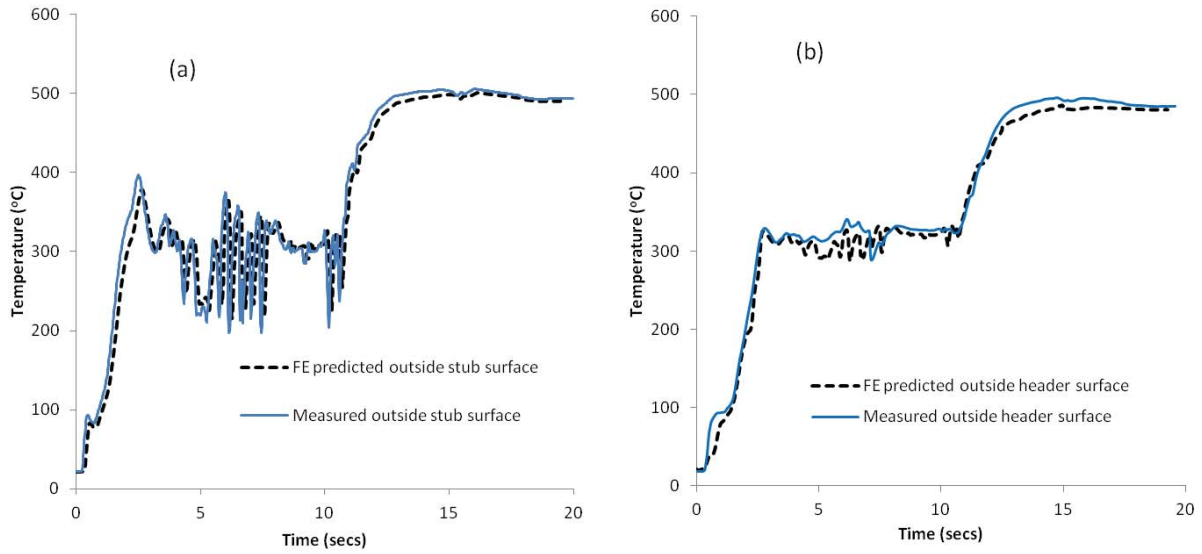


Figure 8. Comparison between (a) measured outside stub surface temperature and the predicted surface temperatures of the stub outside surface and (b) measured outside header surface temperature and the predicted header outside surface temperature.

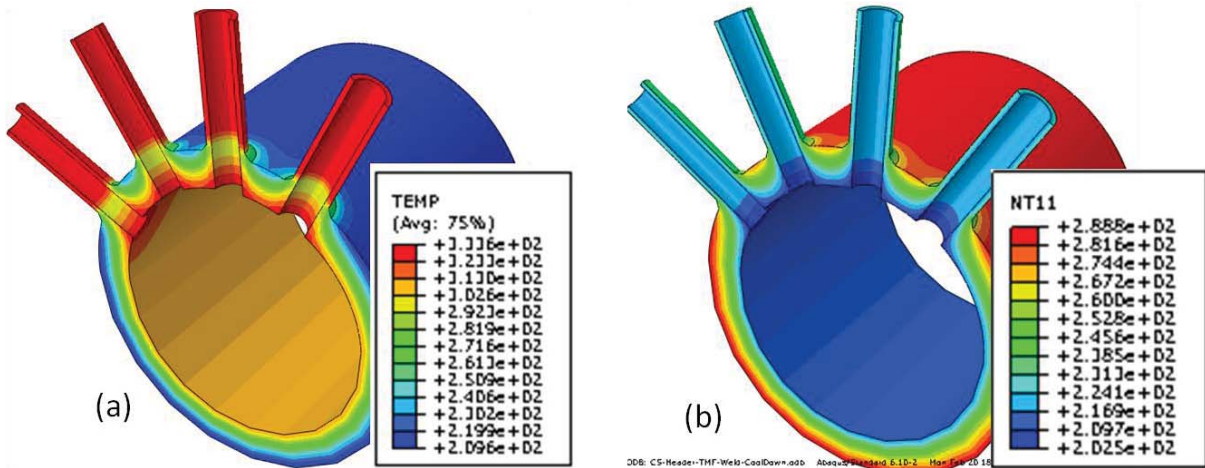


Figure 9. (a) Predicted global model temperature distribution at time H₁. (b) Predicted global model temperature distribution at time C₁.

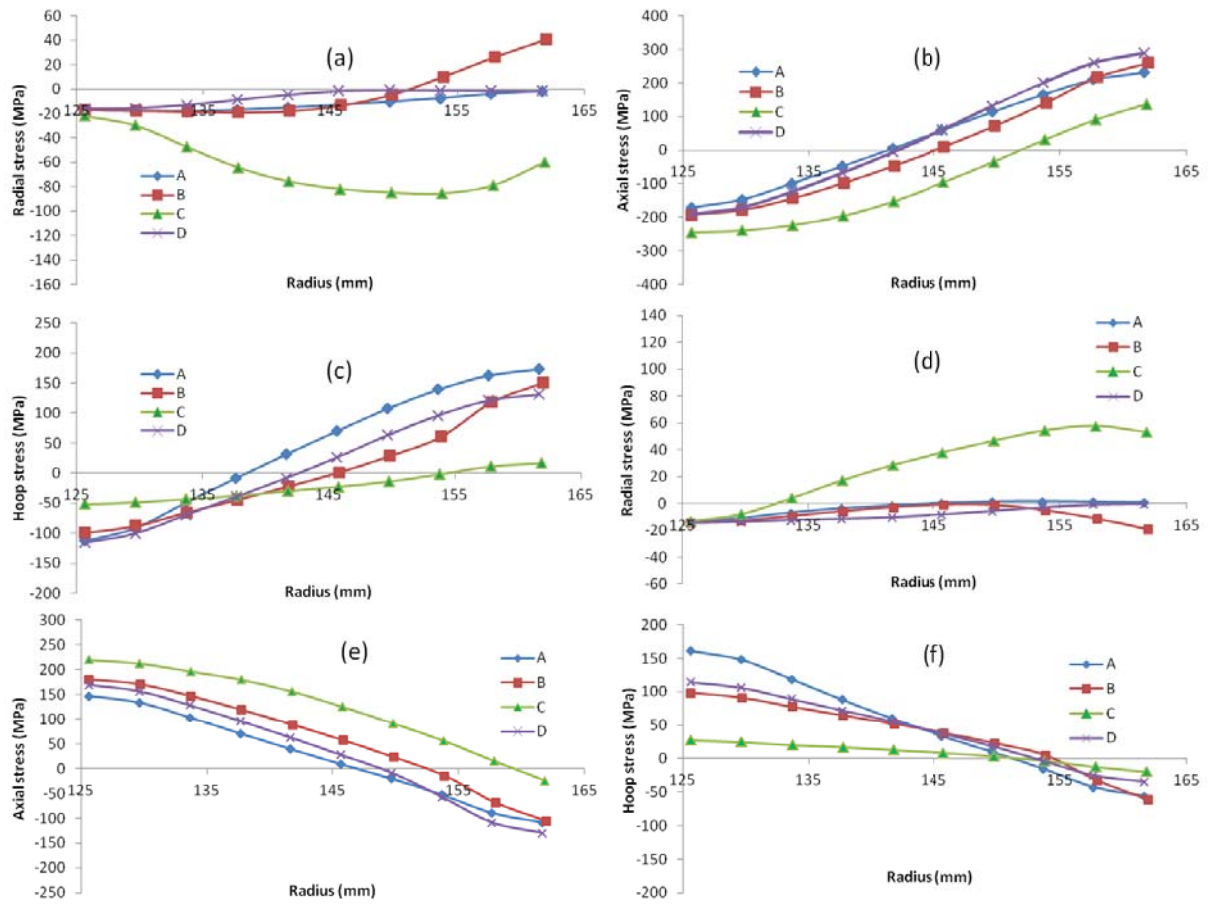


Figure 10. Predicted stress distributions along paths A to D from elastic-viscoplastic analyses for realistic cycle at time H_1 (a to c) and C_1 (d to f).

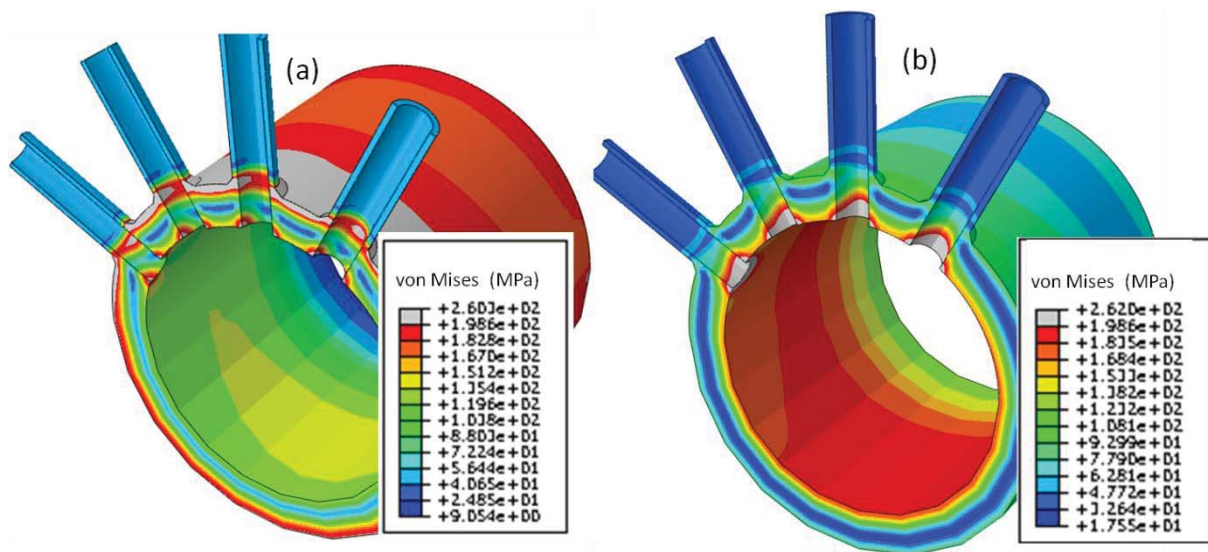


Figure 11. Predicted global model von Mises stress distributions using elastic-viscoplastic material model at times (a) H_1 and (b) C_1 .

1
2
3
4
5
6
7
8
9
10
11
12
13
14
15
16
17
18
19
20
21
22
23
24
25
26
27
28
29
30
31
32
33
34
35
36
37
38
39
40
41
42
43
44
45
46
47
48
49
50
51
52
53
54
55
56
57
58
59
60
61
62
63
64
65

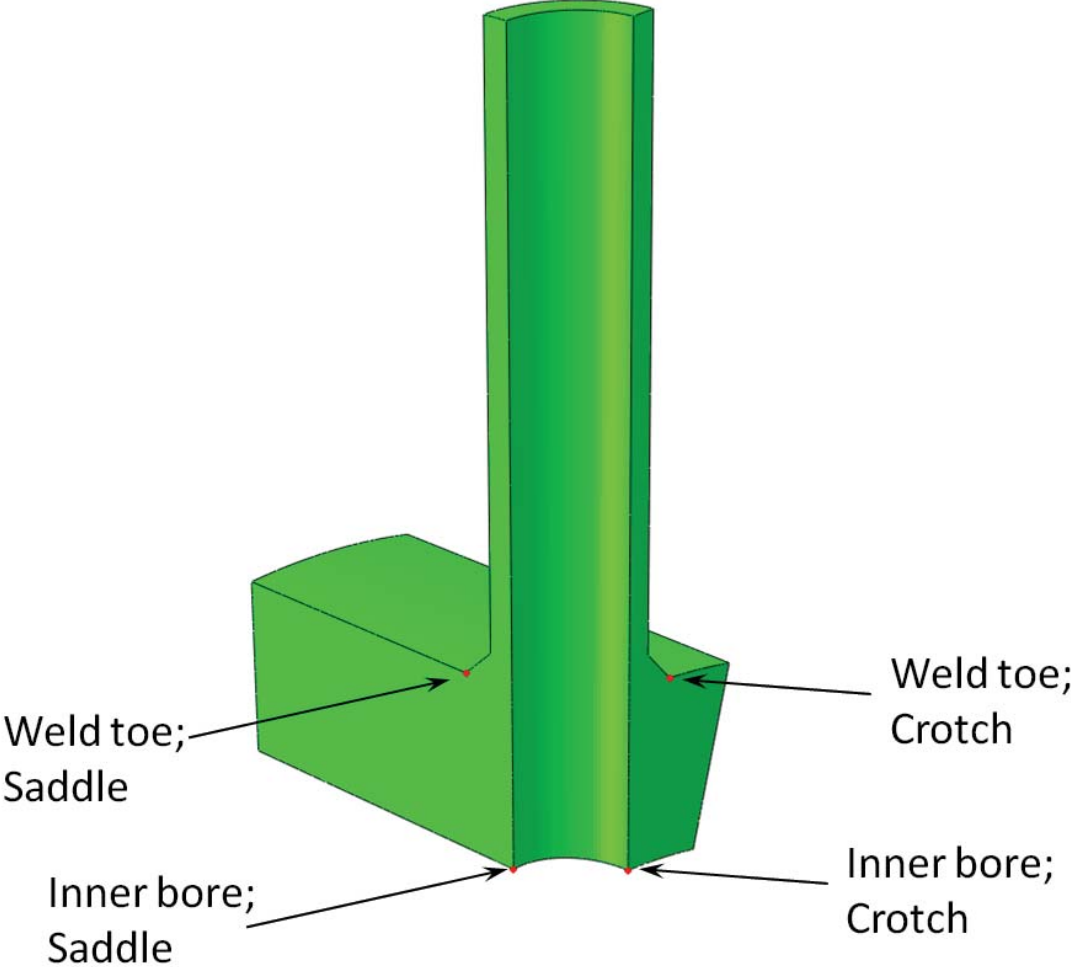


Figure 12. Position of areas of interest within the submodel

1
2
3
4
5
6
7
8
9
10
11
12
13
14
15
16
17
18
19
20
21
22
23
24
25
26
27
28
29
30
31
32
33
34
35
36
37
38
39
40
41
42
43
44
45
46
47
48
49
50
51
52
53
54
55
56
57
58
59
60
61
62
63
64
65

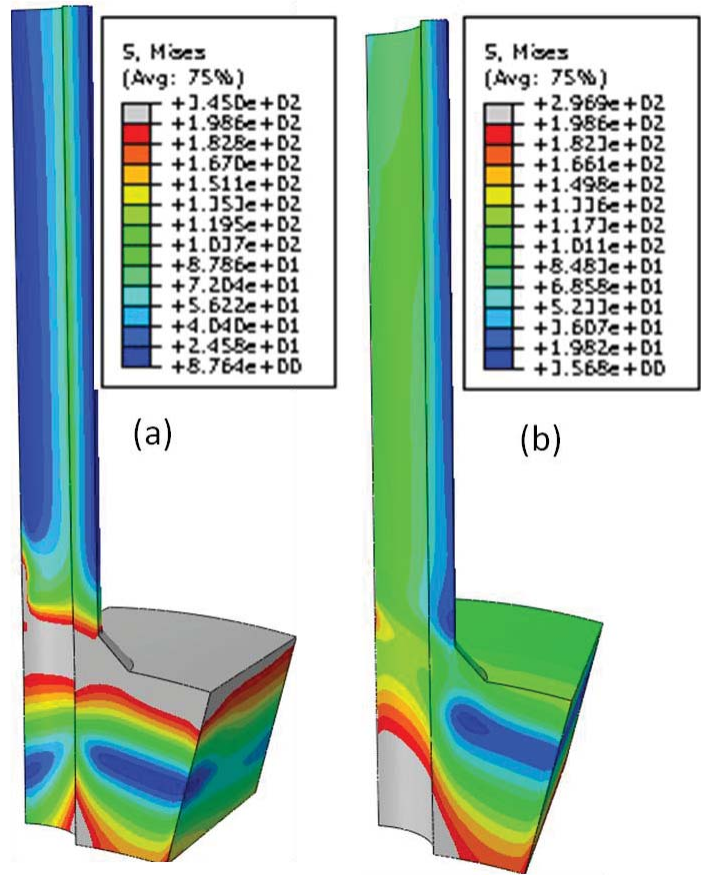


Figure 13. Predicted sub-model von Mises stress distributions at time H_1 : (Fig. 13a) and time C_1 (Fig. 13b).

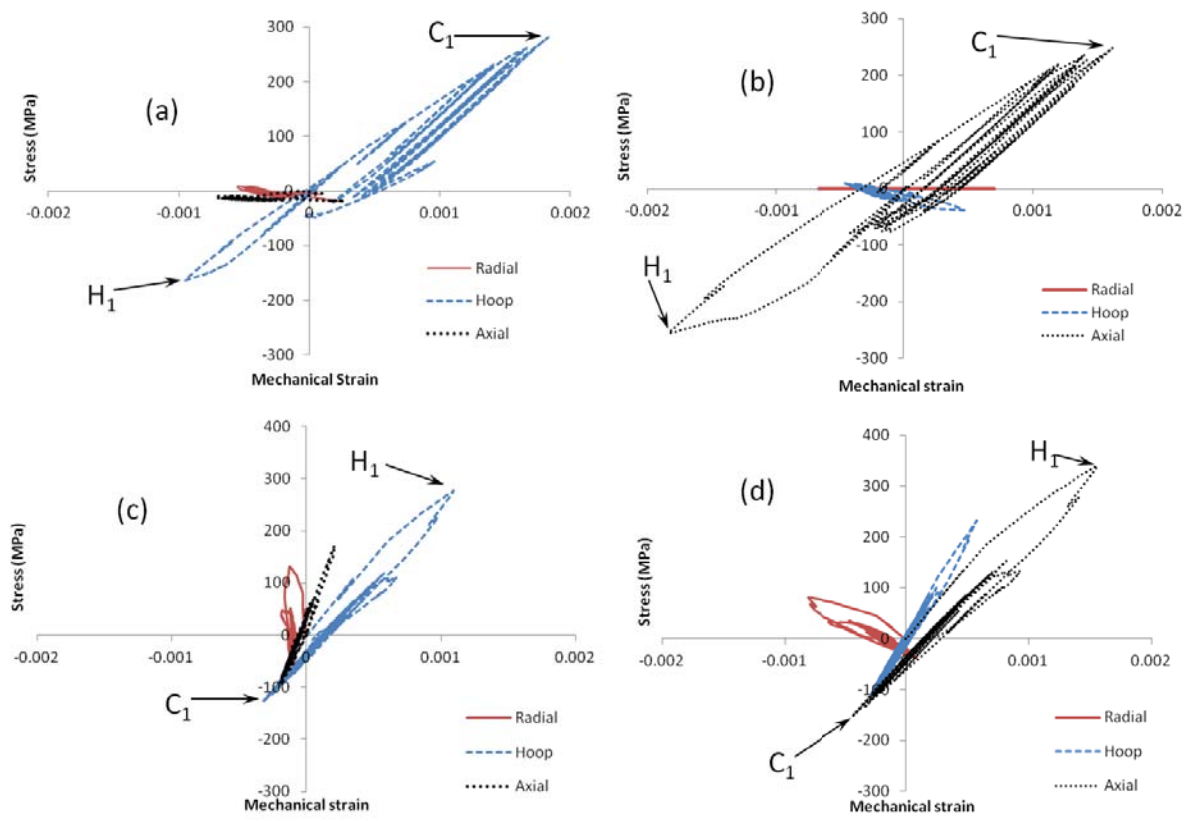


Figure 14. FE-predicted (sub-model) thermo-mechanical stress-strain responses at various locations on header-tube junction for realistic plant cycle (Fig 1): (a) Inner bore - saddle position, (b) Inner bore - crotch position, (c) Weld toe - saddle position, (d) Weld toe - crotch position.

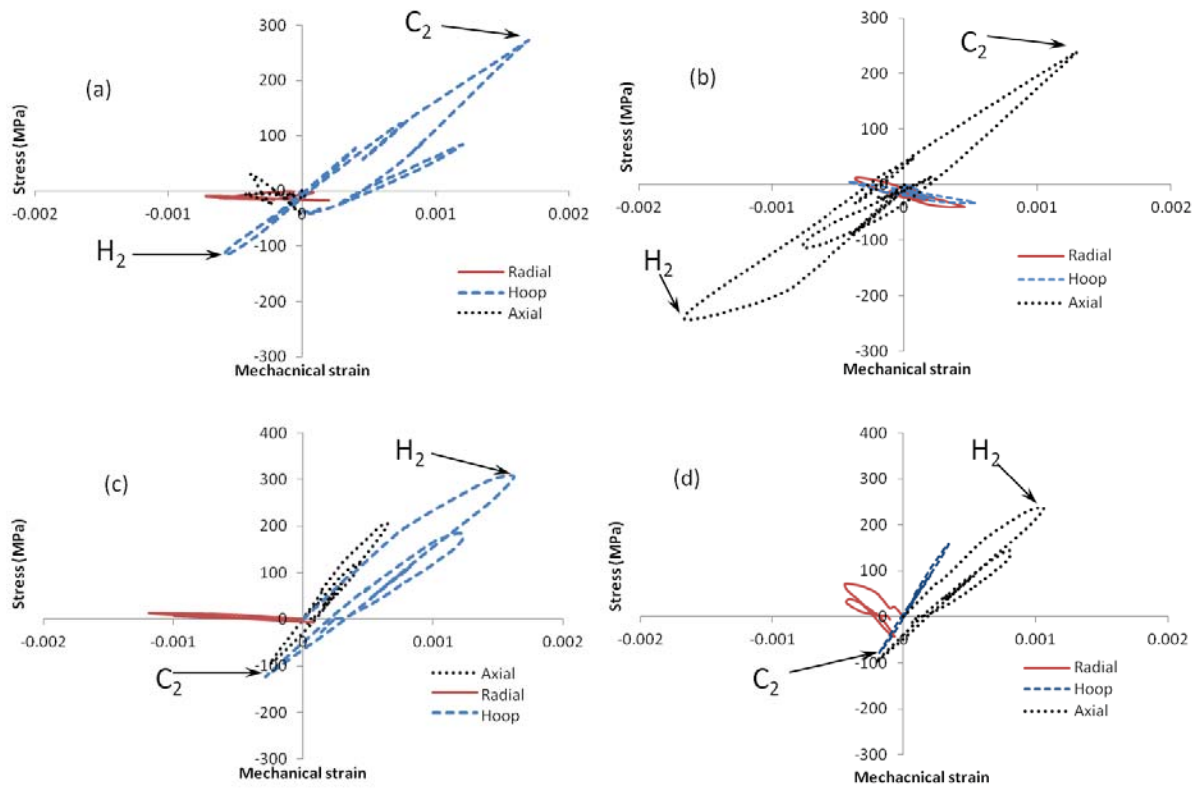


Figure 15. FE-predicted (sub-model) thermo-mechanical stress-strain responses at various locations on header-tube junction for representative plant cycle (Figure 2): (a) Inner bore - saddle position, (b) Inner bore - crotch position, (c) Weld toe - saddle position, (d) Weld toe - crotch position.